A&A 676, A45 (2023)
https://doi.org/10.1051/0004-6361/202345979

Astronomy & Astrophysics
Special issue

Solar Orbiter First Results (Nominal Mission Phase)

In-flight radiometric calibration of the Metis Visible Light channel using stars and comparison with STEREO-A/COR2 data

Y. De Leo[1,2], A. Burtovoi[3], L. Teriaca[1], M. Romoli[3,4], P. Chioetto[5,6], V. Andretta[7], M. Uslenghi[8], F. Landini[9], R. Susino[9], M. Pancrazzi[9], F. Frassati[9], M. Giarrusso[4,10], S. Giordano[9], L. Zangrilli[9], D. Spadaro[10], L. Abbo[9], A. Bemporad[9], G. Capobianco[9], G. E. Capuano[2,10], C. Casini[5,6], M. Casti[11], A. J. Corso[5], V. Da Deppo[5,12], M. Fabi[13,14], S. Fineschi[9], F. Frassetto[5,9], C. Grimani[13,14], S. L. Guglielmino[10], P. Heinzel[15,16], G. Jerse[17], A. Liberatore[18], E. Magli[19], G. Massone[9], M. Messerotti[17], J. D. Moses[20], G. Naletto[21], G. Nicolini[9], M. G. Pelizzo[22], P. Romano[10], G. Russano[7], C. Sasso[7], U. Schühle[1], T. Straus[7], A. Slemer[5], M. Stangalini[23], D. Telloni[9], C. A. Volpicelli[9], and P. Zuppella[5]

(Affiliations can be found after the references)

Received 23 January 2023 / Accepted 24 April 2023

ABSTRACT

Context. We present the results for the in-flight radiometric calibration performed for the Visible Light (VL) channel of the Metis coronagraph on board Solar Orbiter.

Aims. The radiometric calibration is a fundamental step in building the official pipeline of the instrument, devoted to producing the calibrated data in physical units (L2 data).

Methods. To obtain the radiometric calibration factor ($\epsilon_{\rm VL}$), we used stellar targets transiting the Metis field of view. We derived $\epsilon_{\rm VL}$ by determining the signal of each calibration star by means of the aperture photometry and calculating its expected flux in the Metis band pass. The analyzed data set covers the time range from the beginning of the Cruise Phase of the mission (June 2020) until March 2021.

Results. Considering the uncertainties, the estimated factor ϵ_{VL} is in a good agreement with that obtained during the on-ground calibration campaign. This implies that up to March 2021 there was no measurable reduction in the VL channel throughput. Finally, we compared the total and polarized brightness visible light images of the solar corona acquired with Metis and STEREO-A/COR2 during the November 2020 superior conjunction of these instruments. A general good agreement was obtained between the images of these instruments for both the total and polarized brightness.

Key words. Sun: corona

1. Introduction

Metis is the coronagraph on board the ESA/NASA Solar Orbiter mission (Müller et al. 2020), designed to perform simultaneous imaging of the off-limb solar corona with high temporal and spatial resolution, in both visible and ultraviolet light. Metis features two channels: the so-called Ultra Violet (UV) channel in the narrowband H I Lyman-α line at 121.6 ± 10 nm (hereafter H I Ly-α) and the Visible Light (VL) channel in the broad band between 580 and 640 nm (Antonucci et al. 2020; Fineschi et al. 2020). The simultaneous acquisition of the two channels allows us to trace the global dynamics and evolution of the hydrogen component in the solar atmosphere from 1.7 $R_\odot$ to 9 $R_\odot$, by combining the visible light and the ultraviolet frames. The acquisition of polarized brightness (pB) images ensures that the measured signal is caused by electron scattering (due to K-corona) and not by dust particle scattering (due to F-corona), the effect of which becomes prevalent with increasing heliocentric distance (Blackwell & Petford 1966). From the visible light frames it is possible to derive maps of the coronal electron density profiles by using various techniques (see, e.g., van de Hulst 1950; Hayes et al. 2001; Quémerais & Lamy 2002 and references therein). The coronal emission at 121.6 nm is mostly due to neutral hydrogen resonant scattering of the chromospheric H I Ly-α photons (Gabriel 1971). Thus, from the ultraviolet frames, we can derive the maps of the solar wind velocity by means of the Doppler dimming effect: namely, the decrease in the ultraviolet emission from the expanding corona relative to a static one (Noci et al. 1987; Withbroe et al. 1982). The ultraviolet emission of the static corona is simulated starting from the electron density of the plasma inferred from the polarized visible light images (Romoli et al. 2021).

This work is focused on the radiometric calibration of the VL channel and its comparison with the Sun Earth Connection Coronal and Heliospheric Investigation (SECCHI) COR2 instrument (Howard et al. 2008) aboard the Solar Terrestrial Relations Observatory (STEREO). The radiometric calibration is necessary for obtaining the absolute brightness of the solar corona from the imaging data acquired with the VL channel during the several phases of the mission. Furthermore, it allows us to monitor the aging of the VL channel, starting from the beginning of the Cruise Phase of Solar Orbiter. Besides the calibration and characterization activities already performed on the ground, we use stellar target transits across the instrument field of view (FoV) to infer the radiometric calibration factor, $\epsilon_{\rm VL}$. Star observations have been extensively used to calibrate space-based instruments, and a significant heritage exists on this topic, such as the in-flight calibration campaigns of the following coronagraphs: the Large Angle Spectrometric COronagraph (LASCO-C2; Brueckner et al. 1995; Colaninno & Howard 2015) on board

Table 1. Stellar targets used for the radiometric calibration.

Star ID	Spectral type	U	V	R	Observation date	d_{Metis}	Coeff. $R_T \pm \sigma_{R_T}$	$\epsilon_{\mathrm{VL},*} \pm \sigma_*$
α Leonis	B8IVn	0.88	1.40	1.37	15 June 2020	0.51 au	1.14 ± 0.05	0.0126 ± 0.0007
ρ Leonis	B1Iab	2.78	3.87	3.90	17 June 2020	0.52 au	1.13 ± 0.04	0.0140 ± 0.0010
ν Scorpii	B2V	3.42	4.00	3.90	15 March 2021	0.64 au	1.16 ± 0.05	0.0141 ± 0.0006
β01 Scorpii	B1V	1.68	2.62	2.60	15 March 2021	0.64 au	1.16 ± 0.05	0.0141 ± 0.0006
ω Scorpii	B1V	3.10	3.97	3.91	15 March 2021	0.64 au	1.16 ± 0.05	0.0128 ± 0.0014
λ Librae	B3V	4.43	5.03	5.00 [(a)]	15 March 2021	0.64 au	1.15 ± 0.05	0.0137 ± 0.0011
θ Ophiuchi	OB	2.18	3.26	3.38	25 March 2021	0.71 au	1.15 ± 0.04	0.0136 ± 0.0008

Notes. The Johnson-Cousins U, V, R apparent magnitudes of the target stars are listed in the third, fourth and fifth column. Starting date of the target observations is in the sixth column. Distances of Metis d_{Metis} to the Sun in astronomical unit (au), at the time of the observations, are in the seventh column. Values of the coefficient R_T and its σ_{R_T} (error propagation) in the eighth column (see Sect. 2.3). Values of the radiometric calibration factor for every star and its σ_* (standard deviation) are in the last column. Reported information is taken from the SIMBAD catalog, with the exceptions of the last four columns. [(a)]Value derived taking into account the spectral type of the star and the B and V apparent magnitudes. This magnitude is consistent with the value provided by the *Gaia* catalog for the red band pass (Gaia Collaboration 2016, 2023).

the Solar and Heliospheric Observatory (SOHO; Domingo et al. 1995), COR2 (Baldwin & Vourlidas 2008), LASCO-C3/SOHO (Thernisien et al. 2006), and the UltraViolet Coronagraph Spectrometer/SOHO (UVCS; Romoli et al. 2002).

The procedure (pipeline) to obtain calibrated data (level 2 or L2 data), for both channels of Metis, consists of a "chain" of operations applied to the images acquired on board (L0 data). The images are first dark-, bias-, and flat-field-corrected (measured in-flight) and corrected for the vignetting pattern (measured on the ground). Then the signal is transformed into count rates by dividing it by the exposure time. The obtained radiometric calibration factor, ϵ_{VL}, is finally used to convert the observed digital numbers (DNs) per pixel into photons and to express the calibrated frames in radiance (photons $\mathrm{m}^{-2}\ \mathrm{sr}^{-1}\ \mathrm{s}^{-1}$). The L2 final data expressed in mean solar brightness (MSB) units are obtained by dividing the calibrated frames by the average surface brightness of the solar disk in the wavelength range of the instrument. The latter is provided in the header of the correspondent L2 data. After this procedure, for the VL channel, the total brightness, tB, and the polarized brightness, pB, frames are produced by using the theoretical Müller demodulation matrix (Antonucci et al. 2020; Capobianco et al. 2018; Casti et al. 2019; Fineschi et al. 2020; Liberatore et al. 2023). The L2 data also contain the uncertainty matrix, which takes the full error propagation from the steps mentioned above into account.

The calibration performed using star targets, with known and stable fluxes, is a way to measure the in-flight radiometric response of the VL channel and its variation over time with astronomical sources as "standard candles" and represents a key measurement for deriving quantitative information from the solar corona observations. Furthermore, stars, being point sources, are ideal for verifying the instrumental spatial resolution because they provide information on the point spread function (PSF).

The in-flight calibration is described in Sect. 2, and the comparison of the Metis data with those of COR2 is reported in Sect. 3. The main results and conclusions are summarized in Sect. 4.

2. The VL channel radiometric calibration factor

This section explains the method used to infer the value of the radiometric calibration factor ϵ_{VL} (in DN/photon). The data used for this analysis cover a time range from June 2020 (observations of α and ρ Leonis) until March 2021 (observation of θ Ophiuchi), as reported in Table 1.

2.1. Availability of the stellar targets

The in-flight radiometric calibration of the two channels of Metis uses observations of stellar targets that pass across the FoV.

An accurate study on the availability of calibrating stellar targets was performed already before the launch of Solar Orbiter, on 10 February 2020. For this we took into account the peculiar orbit of Solar Orbiter by using the ESA/NASA Spacecraft, Planet, Instrument, C-matrix (pointing), and Events (SPICE) toolkit and considering the instrument characteristics (Focardi et al. 2014). Such an analysis has to be refined after each spacecraft orbital correction (e.g., after gravity-assisted maneuvers).

Due to its band pass (BP, 580–640 nm), the VL channel of Metis can be considered as a nonstandard red filter and, thus, is able to detect a significant amount of stars. As the instrument cannot acquire images at all times due to the telemetry constraints of an interplanetary mission, the choice of the available targets was driven by the overall needs of the Metis radiometric calibration campaigns, which prioritizes the observation of stars suitable for the calibration of the UV channel (see De Leo et al., in prep.). Having a band pass of 121.6 ± 10 nm, Metis UV channel is expected to detect sufficient signal from bright stars of early spectral types, namely O and B. These stars have very stable ultraviolet spectra (Mihalas & Binney 1981) and, hence, are suitable for the calibration of ultraviolet instruments such as the Metis UV channel. Thus, the few available calibration campaigns have been scheduled to cover the transits of these kinds of stars.

The Metis team developed a tool for recognizing possible stellar targets, for plotting the expected stellar tracks on the FoV, and for retrieving useful quantities (stellar type, magnitude) via SIMBAD[1] (Wenger et al. 2000) queries. The tool uses the Metis boresight coordinates (RA and Dec) and the size of the square FoV ($\pm 2.9°$ in width, $\pm 3.4°$ in the diagonal directions) to query the SIMBAD catalog and, then, it returns the stars coordinates in the sensor frame (2048×2048 pixels). The stellar objects observed during the Metis in-flight radiometric campaigns and used for the calibration of the VL channel are listed in Table 1, whereas their tracks within the FoV are shown in Fig. 1. Some of the tracks are not complete due to limitations in the Solar Orbiter observing plan. Besides the targets acquired during the dedicated calibration campaigns that are selected for their suitability, other stars are detected by the VL channel during normal

[1] https://simbad.u-strasbg.fr/simbad/sim-fid

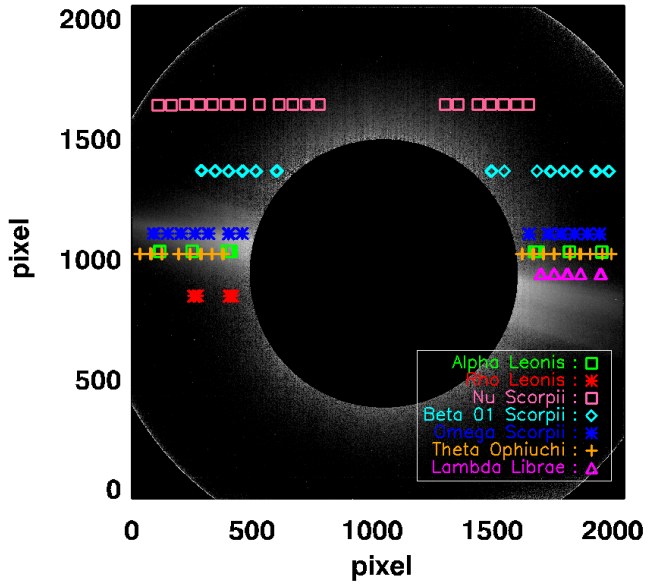

Fig. 1. Map of the tracks of the stellar targets along the Metis VL FoV. The indicated stars make up the data set used to infer the radiometric calibration factor, ϵ_{VL}.

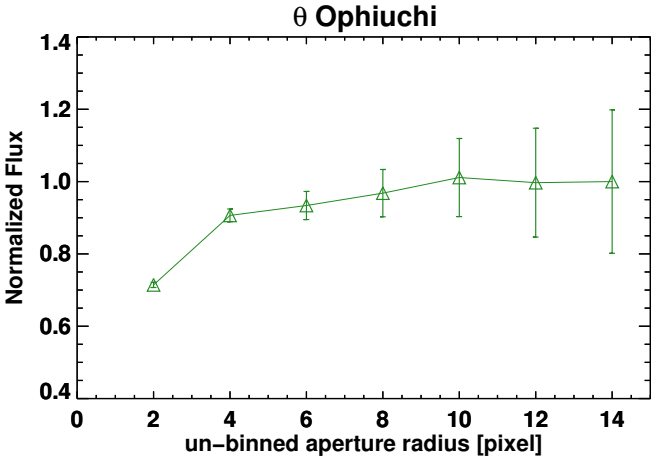

Fig. 2. Measured stellar flux as a function of the aperture radius in pixels.

science operations. Because these targets are acquired in observations not planned for calibration, they are of limited use and are not used for this work.

2.2. Aperture photometry

Once the frames from the radiometric calibration observations are acquired and preprocessed, it is possible to evaluate the star signal using the aperture photometry method. The frame preprocessing consists of the removal of dark and bias, corrections for flat-field and vignetting function (VF), and the normalization for the exposure time.

The star count rate is obtained by summing the signal (DN) falling into a circular area of radius r_1 pixels around the center of the star image after subtracting the average coronal background (evaluated by averaging the signal in DN in the annular area of inner radius r_1 pixels and outer radius r_2 pixels).

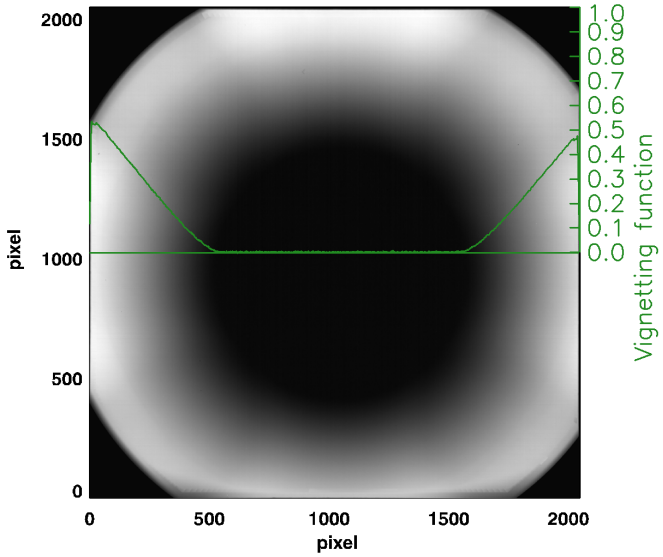

Fig. 3. Map of the VF measured on the ground and its trend along the equatorial direction (solid line in green).

The determination of the best choice for the circular area radius r_1 took into account the PSF of the instrument and, when applicable, the binning factor of the considered frame. Considering that the full width half maximum of the Metis PSF ranges from 1.5 to 3 pixels throughout the FoV in the VL channel (Da Deppo et al. 2021), we chose a radius r_1 of eight pixels for our measurements. In case of data binned aboard, r_1 and r_2 have been divided by the binning factor of the frame. The outer radius r_2 was set to 12 pixels (value for the case of no binning).

Figure 2 shows the stellar flux growth as a function of the photometry radius. The variation in the star signal is about a few percent in the neighborhood (8 ± 2 pixels) of the chosen value of the aperture.

Another important step of the frame processing before proceeding with the calibration is the VF correction. One characteristic of externally occulted coronagraphs is that their FoV is highly vignetted (see Fig. 3). Thus, a correction for the VF is required, to remove the artificial variation of the stellar flux along its track on the FoV. The VF map was measured during the on-ground calibration campaign (Antonucci et al. 2020) and was corrected after the in-flight adjustment of the internal occulter (Liberatore et al. 2021).

We checked that the values of the star signal along the FoV are in good agreement with the VF trend for every considered data set. As an example, Fig. 4 (left panel) shows the signal of β 01 Scorpii along the FoV of the VL channel and the values of the VF. The right panel of Fig. 4 shows the star signal corrected for the VF trend: the general trend is the expected one, except for a few points with a decreasing trend close to the inner limit of the FoV. The star observations give a relative measurement of the VF, and indeed a deviation from the pre-flight VF measurement is the likely explanation for the non-uniformities shown in Fig. 4 (this effect will be discussed in Sect. 2.5).

2.3. The Metis photometric response

The Metis visible light detector assembly (VLDA) consists of a visible light camera equipped with a CMOS active pixel sensor (APS), $2k \times 2k$, $10\,\mu m$ pixel, installed at the end of the

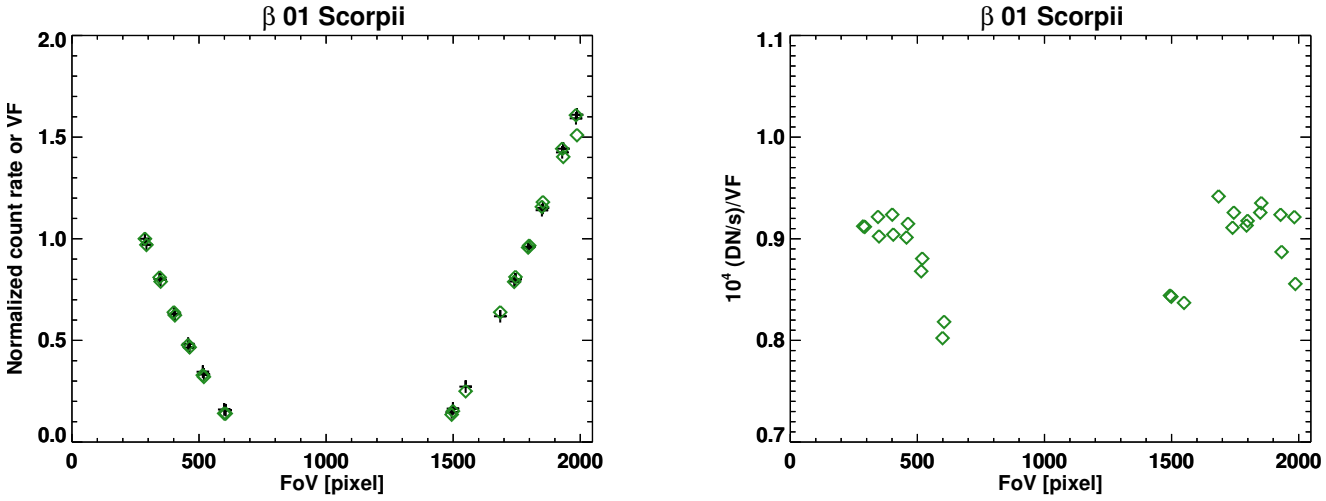

Fig. 4. Aperture photometry results for β 01 Scorpii. Left panel: comparison between the normalized count rate (green diamonds) of β 01 Scorpii and the normalized VF (black crosses). The VF is evaluated in the same positions as the star, along the FoV. Both trends have been normalized to the value of the first frame of this observation. Right panel: trend of the count rate corrected for the VF.

visible light optical path, following the interferential filter assembly (IFA) and the polarimeter assembly. The IFA is an interferential multilayer filter film of Al/MgF_2 deposited on a MgF_2 crystal window, with the optical axis perpendicular to the coated surface. This element has the double purpose of selectively transmitting the H I Ly-α radiation to be detected by the ultraviolet detector assembly, and of reflecting the visible light into the Metis polarimeter that selects the wavelength band 580–640 nm (Antonucci et al. 2020; Casti et al. 2019).

The VL channel can be assimilated to a nonstandard red filter. Thus, in order to determine the fluxes of the radiometric stellar targets, it is necessary to determine the conversion factor between the Metis nonstandard photometric system and a standard one, in this case the Johnson-Cousins (JC) system, for which the stars' photometric data are known (Bessell et al. 1998). The conversion coefficient called R_T is star dependent, and in first approximation, spectral type dependent. R_T is given by the ratio between the averaged flux emitted by the star in the Metis band pass and the averaged flux in the standard JC red filter band pass:

$$R_T = \frac{\overline{f}_{\rm Metis}}{\overline{f}_R}, \tag{1}$$

with averaged fluxes defined as follows:

$$\overline{f}_{\rm Metis} = \frac{\int f_\lambda T_{\rm Metis}\,{\rm d}\lambda}{\int T_{\rm Metis}\,{\rm d}\lambda} \qquad \overline{f}_R = \frac{\int f_\lambda T_R\,{\rm d}\lambda}{\int T_R\,{\rm d}\lambda}, \tag{2}$$

where $T_{\rm Metis}$, T_R are the transmission curves of the Metis BP filter and of the JC red filter, respectively. The transmission curve of the Metis BP filter is reported in Fig. 5.

The evaluation of the coefficient R_T was made by using about 50 synthetic star spectra f_λ from the ESO Library of Stellar Spectra[2], with the aim of deriving the conversion coefficient R_T as a function of the spectral type. Detailed information about the stellar spectra in the catalog can be found in Ivanov et al. (2004). The interstellar extinction and reddening are neglected here because the stellar targets are all in the vicinity of Earth.

[2] https://www.eso.org/sci/facilities/paranal/decommissioned/isaac/tools/lib.html

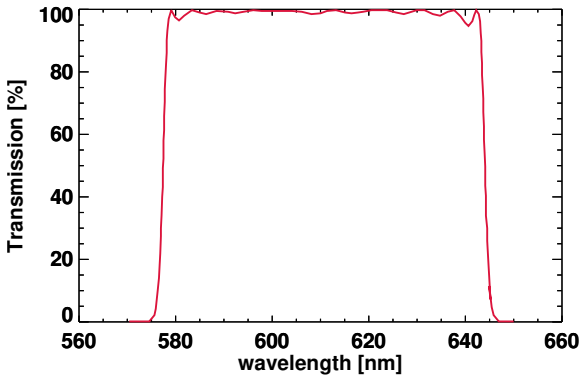

Fig. 5. Transmission curve of the Metis visible light band pass filter.

As a second step, we determined the star flux received by the instrument in the JC red filter band pass for a given star magnitude m_R. To do it we need to know the R band pass flux for stars with null red magnitude, the so-called zero point[3] flux. At this point, the JC red magnitude of a stellar target can be written as

$$m_R - m_{R0} = -2.5 \log \frac{\overline{f}_R}{f_{R0}}, \tag{3}$$

with $\overline{f}_R$ the received flux in the JC R and f_{R0} the zero point flux (Bessell et al. 1998). From Eqs. (1) and (3), we obtain the expected Metis flux for the star:

$$\overline{f}_{\rm Metis} = R_T \cdot \overline{f}_R = R_T \cdot f_{R0} \cdot 10^{\frac{-(m_R - m_{R0})}{2.5}}. \tag{4}$$

Finally, the estimated count rate $N_{\rm VL}$ is

$$N_{\rm VL} = \overline{f}_{\rm Metis} \cdot A_{\rm pup} \cdot VF\,({\rm FoV}) \cdot \epsilon_{\rm VL} \cdot \Delta\lambda_{\rm VL}, \tag{5}$$

where $A_{\rm pup}$ is the pupil area of the telescope, VF is the value of the VF that depends on the pixel coordinates of the frame and $\epsilon_{\rm VL}\cdot\Delta\lambda_{\rm VL}$ is the overall efficiency of the VL channel times the band width defined by the transmission curve of the Metis BP filter.

[3] The "zero point" flux is the main star flux of a photometric calibration system evaluated for each band, which corresponds to the zero magnitude star.

2.4. On-ground calibration

The full system VL channel efficiency has been measured for the first time during the on-ground calibration campaign at the INAF Optical Payload Systems facility (Fineschi et al. 2019). The radiometric response and the VF in the visible light were obtained using a LED flat-field source that illuminated uniformly the entrance pupil and the full Metis FoV. A diode calibrated at US National Institute of Standards and Technology (NIST), equipped with a Metis visible light band pass filter, measures the flat field LED panel light intensity. By combining the measurements of the source with the diode and the Metis telescope, the product of the VF by the VL channel efficiency is obtained, $VF\,(\mathrm{FoV})\cdot\epsilon_{\mathrm{VL}}$. The VF is an adimensional quantity that depends on the pixel coordinates on the frame. It is separated from the visible light efficiency by using a visible light efficiency value determined from the optical elements efficiencies measurements at subsystem level. The value for the visible light efficiency is 0.118 ± 0.022 photo-electrons per photon impinging the entrance pupil (Antonucci et al. 2020). This value can be divided by the detector gain 8.4 ± 0.3 photo-electrons per DN to achieve the visible light efficiency of 0.014 ± 0.003 DN/photon. The in-flight calibration aims at verifying, monitoring and possibly improving this number.

2.5. Data inversion and calibration across the FoV

By considering the star count rate N_{VL}, each star measurement provides the value of the coefficient ϵ_{VL}, which can be derived from Eq. (5):

$$\epsilon_{\mathrm{VL}} = \frac{N_{\mathrm{VL}}\,(\mathrm{FoV})}{\overline{f}_{\mathrm{Metis}}\cdot A_{\mathrm{pup}}\cdot \mathrm{VF}\,(\mathrm{FoV})\cdot\Delta\lambda_{\mathrm{VL}}}. \tag{6}$$

Figure 6 shows the results from the inversion of the data set, which consists of seven stars (see Table 1). For each of them we obtained the values of the ϵ_{VL} related to the positions across the FoV, as a function of radial distance from the center of the internal occulter. The error bars are the standard deviations, σ_*, of the radiometric calibration factor, computed from the data set of each stellar target. The horizontal gray solid line represents the ϵ_{VL} value from the on-ground campaign, the two gray dashed lines delimit the 1σ tolerance range around the central value. The red solid line indicates the ϵ_{VL} value estimated as the average of the whole data set. This value with its standard deviation 1σ is equal to 0.014 ± 0.001 DN/photon. The radiometric calibration factor determined in the vicinity of the occulter (see the black vertical line in Fig. 6) varies with approaching to the inner edge of the FoV. There is a hypothesis that might explain this effect, as described later on. We obtained that the two radiometric calibration factors values are consistent within the uncertainties.

Although the results from the on-ground and the in-flight calibration campaigns are in a good agreement, some of the stellar targets, in particular β 01 Scorpii, ω Scorpii, and θ Ophiuchi, present a clear decreasing trend in the zone nearby the occulter. The most likely explanation of this unexpected trend is an overestimate of the VF, likely due to the presence of stray light nearby the occulter when the throughput of the instrument was measured on-ground. In fact, in the ideal case, a proper correction of the data with VF should result in a constant value of the flux of each star. In addition to this, the star signal is significantly distorted near the occulter due to diffraction making the estimate of the stellar flux more difficult.

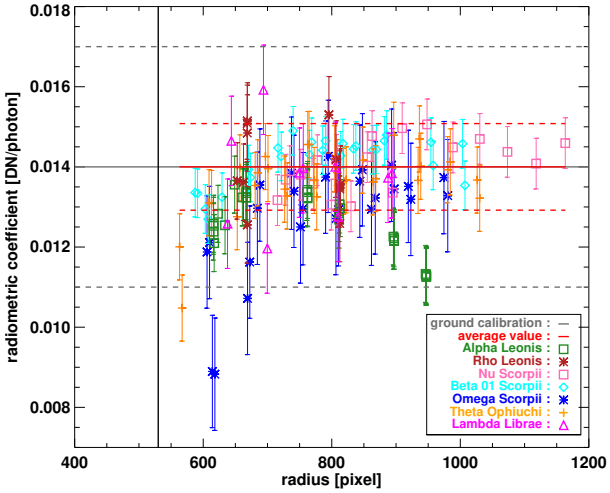

Fig. 6. Radiometric calibration factors as a function of the radial distance of the star images from the center of the occulter. The solid red line is the average value of ϵ_{VL}. The solid gray line represents the on-ground value of the radiometric calibration factor. The dashed gray and red lines depict the uncertainties of the on-ground and in-flight radiometric factors, respectively. The vertical solid black line is the radius of the internal occulter in pixels.

Table 2. Superior conjunction of Metis with COR2.

Parameters of conjunction	
Date	18–21 Nov. 2020
d_{Metis}	0.92 au
d_{COR2}	0.95 au
$\lvert\Delta l_{\mathrm{POS}}\rvert$	<0.41°
$\lvert\Delta b_{\mathrm{POS}}\rvert$	<1.10°
FoV	5.55–11.5 $R_\odot$

Notes. d_{Metis} and d_{COR2} are the distances of two instruments to the Sun in astronomical units (au). $\lvert\Delta l_{\mathrm{POS}}\rvert$ and $\lvert\Delta b_{\mathrm{POS}}\rvert$ are the absolute differences in longitude and latitude of plane of the sky (POS) of Metis and COR2, respectively. FoV represents the overlapping part of the FoVs of two instruments.

3. Comparing coronal visible light images of Metis and COR2

In this section we compare the total and polarized brightness visible light images of the solar corona obtained with Metis by applying the radiometric calibration described above with those obtained with COR2. While a preliminary cross-calibration of Metis VL channel with Mauna Loa Solar Observatory (MLSO) COronal Solar Magnetism Observatory (COSMO) K-coronagraph (K-cor; see, e.g., de Wijn et al. 2012) and LASCO/SOHO coronagraphs was carried out with the first light data (Fineschi et al. 2021), here we present a more detailed comparison of the visible light data, which were acquired during the superior conjunction of Solar Orbiter with STEREO-A on 18–21 November 2020. During this period of time, the distance to the Sun and orientation of the plane of the sky (POS) of Metis and COR2 were similar (see Table 2).

We used Metis tB and pB images of level 2 (L2, data release "V01"), which were acquired using the polarized brightness acquisition mode (Antonucci et al. 2020) and then processed by means of the radiometric calibration procedure described above. The total and polarized brightness images of COR2

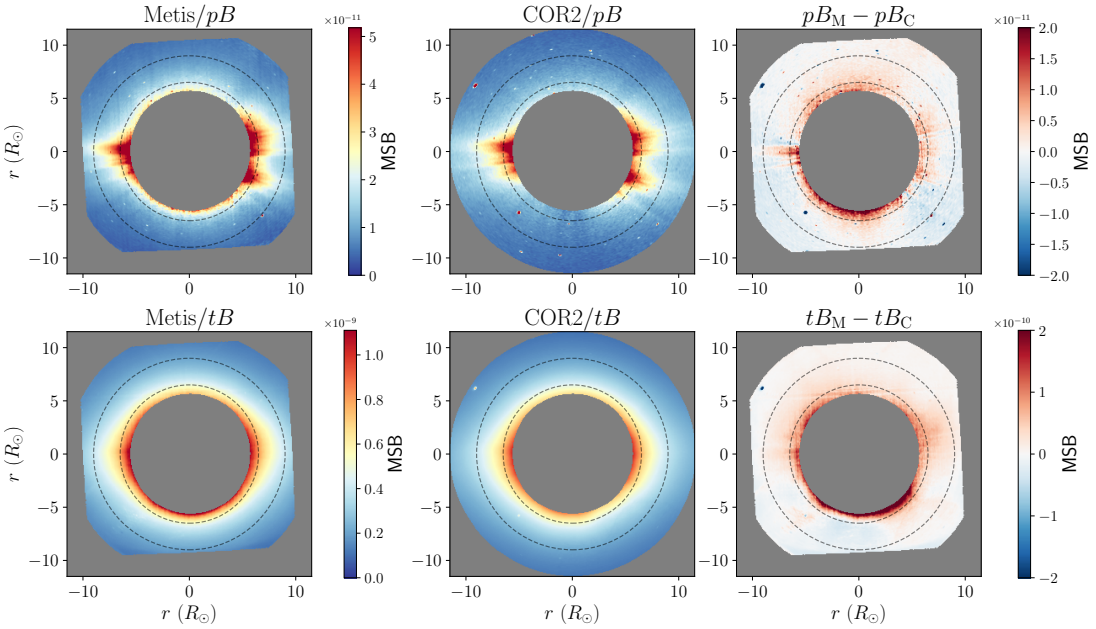

Fig. 7. Polarized (pB) and total (tB) brightness images acquired on 18 November 2020 with Metis at 18:50:36 (left panels) and with COR2 at 18:53:15 (mid panels). The COR2 images are inverted around the N-S axis passing through the Sun center (see the main text for details). Right panels represent the difference between Metis (pB_M and tB_M) and COR2 (pB_C and tB_C) images. The dashed black circles mark the heliocentric distances of 6.5 $R_\odot$ and 9 $R_\odot$, respectively. The color bar represents intensity in MSB units. Horizontal and vertical axes correspond to the heliocentric distance in $R_\odot$ units.

were obtained by performing the standard calibration procedure with the `SolarSoft`[4] package (Freeland & Handy 1998), routine `secchi_prep.pro`. This tool converts a raw signal of COR2 into MSB units considering the band pass of its spectral filter (650–750 nm, Howard et al. 2008) and the photometric calibration factor, which was obtained observing numerous stars (for details, see STEREO/SECCHI Calibration and Measurement Algorithms Documents[5]).

In order to unify the format of different images, we oriented them in such a way that the northern pole of the Sun points to the top and the west solar equator to the right. We also inverted the COR2 images around the N-S axis passing through the Sun center, since this instrument was observing from the opposite side of the Sun during the superior conjunction with Metis in November 2020. All maps were then converted from Cartesian to polar (r, ϕ) coordinates. For this, we determined a grid of polar coordinates with a step of the radial axis equal to 0.01 $R_\odot$ and that of the polar angle axis equal to 1°. The range of the r-axis is defined by the size of the overlapping part of the FoVs of Metis and COR2 (see Table 2). The polar angle ϕ is measured counterclockwise from the west solar equator. The intensity at each pixel of the polar coordinate grid was estimated by means of a B-spline interpolation of order 1 (Briand & Monasse 2018) of the surrounding pixels of the original image.

An example of the resulting total and polarized brightness images acquired quasi-simultaneously with Metis and COR2 is shown in Fig. 7. These images were converted back to Cartesian coordinates for better visualization. The corresponding latitudinal profiles at the heliocentric distance of 6.5 $R_\odot$ and 9 $R_\odot$ can be found in Fig. 8, where we also show the error bars of the pB and tB values. The relative uncertainties of the COR2 data were taken equal to ±20% as suggested in Frazin et al. (2012), whereas those of the Metis data were estimated propagating errors from the various steps of the calibration procedure mentioned in Sect. 1.

Although the band pass of COR2 differs from that of Metis, the comparison of the pB images of these instruments represented in the fraction of MSB has been carried out directly. At the considered heliocentric distances, the polarized emission is dominated by the K-corona, which originates through the Thomson scattering of photospheric light by free electrons. Since the Thompson cross section does not depend on wavelength, the fraction of light (expressed in MSB) scattered within the band pass of Metis is the same as that of COR2. We found that the polarized brightness images of Metis (pB_M) and COR2 (pB_C) are in a good agreement (see the top panels of Fig. 7). For example, we obtained that the average difference of pB intensities at 6.5 $R_\odot$ (Fig. 8, top left panel) is equal to $(3.3 \pm 3.6) \times 10^{-12}$ MSB. This estimate corresponds to the mean and the standard deviation of the distribution of $\Delta pB_{6.5\,R_\odot} = (pB_M - pB_C)$ values. The relative difference, calculated as a ratio of $\Delta pB_{6.5\,R_\odot}$ and the amplitude of the pB_M profile, is equal to 7.0% ± 7.7%. At heliocentric distances of 9 $R_\odot$ (Fig. 8, top right panel), $\Delta pB_{9\,R_\odot}$ is equal to $(-0.71 \pm 1.57) \times 10^{-12}$ MSB, which corresponds to lower relative difference: −3.5% ± 7.7%. The increase of ΔpB at low altitudes can be explained by the presence of an additional component (e.g., stray light) close to the inner part of the Metis FoV. The detailed investigation of this component is beyond the original scope of this paper and is left for future studies.

The direct comparison of the total brightness is less straightforward due to the presence of the stray light in both instruments. In addition, tB images of Metis and COR2 most probably have a different contribution from the F-corona within their band passes, which arises from the wavelength-dependent scattering of the photospheric emission on the dust grains. As can be seen from Figs. 7 and 8 (bottom left panel), the Metis tB image is on average brighter than that of COR2 at low heliocentric distances

[4] www.lmsal.com/solarsoft/
[5] https://stereo-ssc.nascom.nasa.gov/publications/CMAD/secchi/

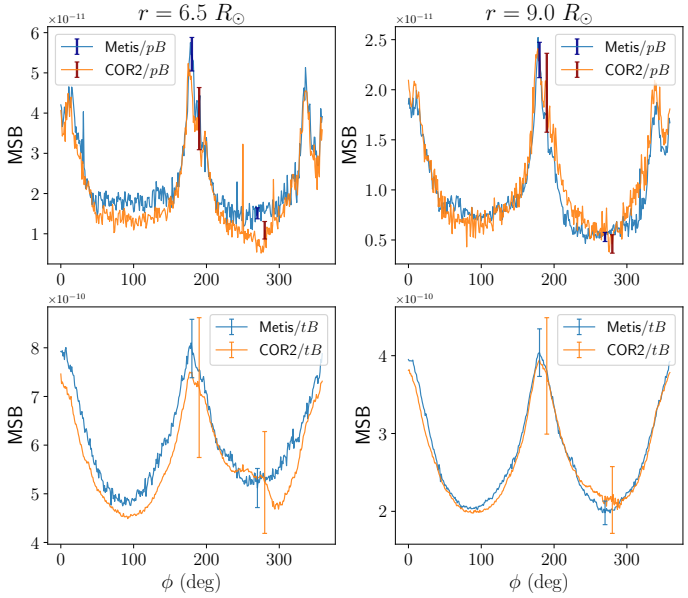

Fig. 8. Latitudinal profiles of the pB (top panels) and tB images (bottom panels) of Metis and COR2 shown in Fig. 7 at the heliocentric distance of 6.5 $R_\odot$ (left panels) and 9 $R_\odot$ (right panels). The blue and orange lines show profiles of Metis and COR2, respectively. The error bars represent the uncertainties of the considered data (see the main text for details).

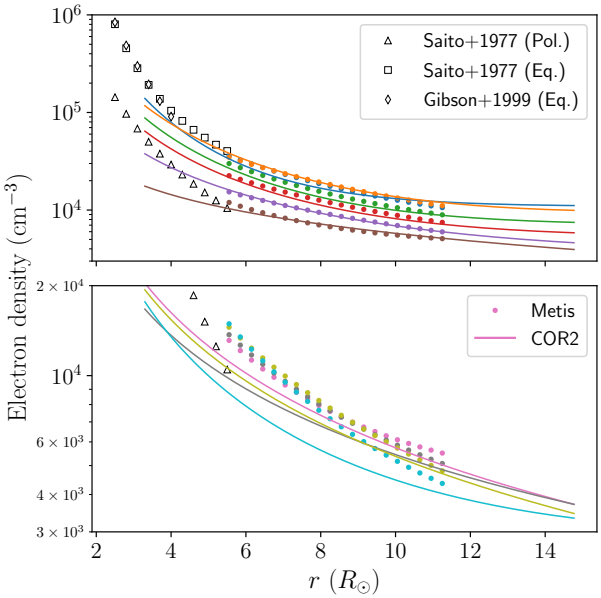

Fig. 9. Radial electron density profiles calculated by inverting the pB images shown in Fig. 7. The profiles of Metis and COR2 are depicted by the filled circles and solid lines, respectively. The colors represent different angles: blue ($\phi = 0°$), orange ($\phi = 10°$), green ($\phi = 20°$), red ($\phi = 30°$), purple ($\phi = 40°$), brown ($\phi = 50°$), pink ($\phi = 60°$), gray ($\phi = 70°$), olive ($\phi = 80°$), and cyan ($\phi = 90°$). The COR2 profiles are calculated for the whole FoV of the instrument (3.3–14.8 $R_\odot$). The polar (Pol.) and equatorial (Eq.) electron density profiles reported in Saito et al. (1977) and that of the equatorial region reported in Gibson et al. (1999) are shown for comparison as black triangles, squares, and diamonds, respectively.

($\lesssim 8\ R_\odot$). The COR2 image, in turn, clearly contains the stray light component at $\phi \approx 270°$. The absolute and relative differences of the total brightness profiles of Metis (tB_M) and COR2 (tB_C) at 6.5 $R_\odot$ are $(3.8 \pm 2.8) \times 10^{-11}$ MSB and 11.4% ± 8.3%, respectively. These features become less evident at higher heliocentric distances, where the contamination of the stray light is expected to be lower. We found that latitudinal tB profiles of the two instruments are rather similar at heliocentric distances $\gtrsim 8\ R_\odot$. The absolute and relative values of ΔtB calculated for the latitudinal profiles at 9 $R_\odot$ (Fig. 8, bottom right panel) are equal to $(4.5 \pm 9.5) \times 10^{-12}$ MSB and 2.2% ± 4.6%, respectively.

Finally, we calculated the electron density profiles (n_e) by applying the inversion technique of van de Hulst (1950) to the whole pB images of Metis (FoV: 5.55–11.5 $R_\odot$) and COR2 (FoV: 3.3–14.8 $R_\odot$). Two sets of n_e profiles extracted from the northwest sector ($0° \leq \phi \leq 90°$) of these quasi-simultaneous images are shown in Fig. 9. We found that values of electron density estimated for the equatorial regions ($\phi \leq 60°$ in Fig. 9) are consistent with each other. In addition, they rather smoothly connect with profiles presented in previous studies (e.g., Saito et al. 1977; Gibson et al. 1999). We note that polar n_e profiles of Metis ($70° \leq \phi \leq 90°$ in Fig. 9) are systematically higher than those of COR2. This is most probably related to the presence of the above-mentioned additional component in the Metis pB data close to the inner part of its FoV, which becomes significant in the polar region where the coronal emission is faint.

4. Conclusions

In this work we present the results of the in-flight radiometric calibration of the VL channel of Metis coronagraph on board Solar Orbiter. The radiometric calibration factor, ϵ_{VL}, was obtained by using planned star observations in the time period from June 2020 until March 2021. The value of the coefficient is equal to 0.014 ± 0.001 DN/photon across the full FoV, and it is consistent, within the uncertainties, with the value of 0.014 ± 0.003 DN/photon from the on-ground calibration campaign. Currently, the factor ϵ_{VL} is used in the official pipeline of Metis, which produces calibrated (L2) data. The radiometric calibration of the UV channel of Metis is left to a forthcoming work. As the results from all stellar targets are consistent, within the uncertainties, with one another and with the ground calibration, we conclude that no degradation of the channel response has occurred (up to March 2021).

The values from the data set present an unexpected trend near the occulter (see Fig. 6). One possible explanation is an undercorrection of the stars' signal in the zone of the images close to the occulter, where our knowledge of the VF is poor (e.g., possibly due to the presence of stray light near the occulter during the on-ground calibration measurements). Nevertheless, the stars that transited across the FoV also served as an in-flight calibration of the VF (Fig. 4, left panel).

We compared the visible light images acquired with Metis and COR2 during the conjunction with Solar Orbiter. The values of the total and polarized brightness of the solar corona measured with these two instruments are found to be in reasonable agreement with one another, even without accounting for the instrumental background (stray light) and likely different contribution of the F-corona to the tB images. In addition, we find that the electron density profiles calculated by inverting the pB images of Metis and COR2 are consistent with one another and also with those reported in the literature. Finally, we note that, after the preliminary cross-calibration reported in Fineschi et al. (2021), comparing the Metis data with those of LASCO acquired during various conjunctions and oppositions with Solar Orbiter is of great interest. However, given the different treatment of the LASCO data (e.g., subtraction of the stray light from tB images and complex optimization of the pB maps of the C2 telescope)

and the larger data set to be analyzed, this work is left to a forthcoming publication.

Acknowledgements. Solar Orbiter is a space mission of international collaboration between ESA and NASA, operated by ESA. The Metis programme is supported by the Italian Space Agency (ASI) under the contracts to the cofinancing National Institute of Astrophysics (INAF): Accordi ASI-INAF N. I-043-10-0 and Addendum N. I-013-12-0/1, Accordo ASI-INAF N.2018-30-HH.0 and under the contracts to the industrial partners OHB Italia SpA, Thales Alenia Space Italia SpA and ALTEC: ASI-TASI N. I-037-11-0 and ASI-ATI N. 2013-057-I.0. Metis was built with hardware contributions from Germany (Bundesministerium für Wirtschaft und Energie (BMWi) through the Deutsches Zentrum für Luft- und Raumfahrt e.V. (DLR)), from the Academy of Sciences of the Czech Republic (Czech PRODEX) and from ESA. Metis team thanks the former PI, Ester Antonucci, for leading the development of Metis until the final delivery to ESA. In this work we made use of the following open source and community-developed `Python` packages: `Matplotlib` (Hunter 2007), `NumPy` (Harris et al. 2020), `SciPy` (Virtanen et al. 2020), `Astropy` (Astropy Collaboration 2013, 2018, 2022) and `SunPy` (The SunPy Community 2020). The SECCHI/COR2 data used here were produced by an international consortium of the Naval Research Laboratory (USA), Lockheed Martin Solar and Astrophysics Lab (USA), NASA Goddard Space Flight Center (USA), Rutherford Appleton Laboratory (UK), University of Birmingham (UK), Max-Planck-Institut for Solar System Research (Germany), Centre Spatiale de Liège (Belgium), Institut d'Optique Theorique et Appliquée (France), and Institut d'Astrophysique Spatiale (France). Y.D.L. acknowledges support by Max-Planck-Institut für Sonnensystemforschung in Göttingen (Germany), the Università degli Studi di Catania (PIA.CE.RI. 2020–2022 Linea 2) and by the Italian MIUR-PRIN grant 2017APKP7T on "Circumterrestrial Environment: Impact of Sun-Earth Interaction". P.H. was partially supported by the grant of the Czech Funding Agency No.22-34841S and by the program "Excellence Initiative – Research University" for University of Wrocław, BPIDUB.4610.96.2021.KG.

References

Antonucci, E., Romoli, M., Andretta, V., et al. 2020, A&A, 642, A10
Astropy Collaboration (Robitaille, T. P., et al. 2013, A&A, 558, A33
Astropy Collaboration (Price-Whelan, A. M., et al.) 2018, AJ, 156, 123
Astropy Collaboration (Price-Whelan, A. M., et al.) 2022, ApJ, 935, 167
Baldwin, K., & Vourlidas, A. 2008, in AGU Fall Meeting Abstracts, 2008, SH13B-1532
Barnes, W. T., Bobra, M. G., et al. 2020, ApJ, 890, 68
Bessell, M. S., Castelli, F., & Plez, B. 1998, A&A, 333, 231
Blackwell, D. E., & Petford, A. D. 1966, MNRAS, 131, 399
Briand, T., & Monasse, P. 2018, Image Processing On Line, 8, 99
Brueckner, G. E., Howard, R. A., Koomen, M. J., et al. 1995, Sol. Phys., 162, 357
Capobianco, G., Casti, M., Fineschi, S., et al. 2018, in Space Telescopes and Instrumentation 2018: Optical, Infrared, and Millimeter Wave, eds. M. Lystrup, H. A. MacEwen, G. G. Fazio, et al., SPIE Conf. Ser., 10698, 1069830
Casti, M., Fineschi, S., Capobianco, G., et al. 2019, in International Conference on Space Optics, ICSO 2018, eds. Z. Sodnik, N. Karafolas, & B. Cugny, SPIE Conf. Ser., 11180, 111803C
Colaninno, R. C., & Howard, R. A. 2015, Sol. Phys., 290, 997
Da Deppo, V., Chioetto, P., Andretta, V., et al. 2021, in International Conference on Space Optics, ICSO 2020, eds. B. Cugny, Z. Sodnik, & N. Karafolas, SPIE Conf. Ser., 11852, 1185210
de Wijn, A. G., Burkepile, J. T., Tomczyk, S., et al. 2012, in Ground-based and Airborne Telescopes IV, eds. L. M. Stepp, R. Gilmozzi, & H. J. Hall, SPIE Conf. Ser., 8444, 84443N
Domingo, V., Fleck, B., & Poland, A. I. 1995, Sol. Phys., 162, 1
Fineschi, S., Casti, M., Capobianco, G., et al. 2019, 2019 IEEE 5th International Workshop on Metrology for AeroSpace (MetroAeroSpace) , 309
Fineschi, S., Naletto, G., Romoli, M., et al. 2020, Exp. Astron., 49, 239
Fineschi, S., Romoli, M., Andretta, V., et al. 2021, in International Conference on Space Optics, ICSO 2020, eds. B. Cugny, Z. Sodnik, & N. Karafolas, SPIE Conf. Ser., 11852, 1185211
Focardi, M., Capobianco, G., Andretta, V., et al. 2014, in Space Telescopes and Instrumentation 2014: Ultraviolet to Gamma Ray, eds. T. Takahashi, J. W. A. den Herder, & M. Bautz, SPIE Conf. Ser., 9144, 914409
Frazin, R. A., Vásquez, A. M., Thompson, W. T., et al. 2012, Sol. Phys., 280, 273
Freeland, S. L., & Handy, B. N. 1998, Sol. Phys., 182, 497
Gabriel, A. H. 1971, Sol. Phys., 21, 392
Gaia Collaboration (Prusti, T., et al.) 2016, A&A, 595, A1
Gaia Collaboration (Vallenari, A. et al.) 2023, A&A, 674, A1
Gibson, S. E., Fludra, A., Bagenal, F., et al. 1999, J. Geophys. Res., 104, 9691
Harris, C. R., Millman, K. J., van der Walt, S. J., et al. 2020, Nature, 585, 357
Hayes, A. P., Vourlidas, A., & Howard, R. A. 2001, ApJ, 548, 1081
Howard, R. A., Moses, J. D., Vourlidas, A., et al. 2008, Space Sci Rev., 136, 67
Hunter, J. D. 2007, Comput. Sci. Eng., 9, 90
Ivanov, V. D., Rieke, M. J., Engelbracht, C. W., et al. 2004, ApJS, 151, 387
Liberatore, A., Fineschi, S., Casti, M., et al. 2021, in International Conference on Space Optics, ICSO 2020, eds. B. Cugny, Z. Sodnik, & N. Karafolas, SPIE Conf. Ser., 11852, 1185248
Liberatore, A., Fineschi, S., Casti, M., et al. 2023, A&A, 672, A14 (SO Nominal Mission Phase SI)
Mihalas, D., & Binney, J. 1981, Galactic Astronomy. Structure and Kinematics (San Francisco: Freeman)
Müller, D., St. Cyr, O. C., Zouganelis, I., et al. 2020, A&A, 642, A1
Noci, G., Kohl, J. L., & Withbroe, G. L. 1987, ApJ, 315, 706
Quémerais, E., & Lamy, P. 2002, A&A, 393, 295
Romoli, M., Frazin, R. A., Kohl, J. L., et al. 2002, ISSI Sci. Rep. Ser., 2, 181
Romoli, M., Antonucci, E., Andretta, V., et al. 2021, A&A, 656, A32
Saito, K., Poland, A. I., & Munro, R. H. 1977, Sol. Phys., 55, 121
Thernisien, A. F., Morrill, J. S., Howard, R. A., & Wang, D. 2006, Sol. Phys., 233, 155
The SunPy Community (Barnes, W. T., et al.) 2020, ApJ, 890, 68
van de Hulst, H. C. 1950, Bull. Astron. Inst. Neth., 11, 135
Virtanen, P., Gommers, R., Oliphant, T. E., et al. 2020, Nat. Methods, 17, 261
Wenger, M., Ochsenbein, F., Egret, D., et al. 2000, A&AS, 143, 9
Withbroe, G. L., Kohl, J. L., Weiser, H., & Munro, R. H. 1982, Space Sci Rev., 33, 17

[1] Max-Planck-Institut für Sonnensystemforschung, Justus-von-Liebig-Weg 3, 37077 Göttingen, Germany
e-mail: `deleo@mps.mpg.de`
[2] University of Catania – Physics and Astronomy Department "Ettore Majorana", Via Santa Sofia 64, 95123 Catania, Italy
[3] INAF – Arcetri Astrophysical Observatory, Largo Enrico Fermi 5, 50125 Florence, Italy
[4] University of Florence – Physics and Astronomy Department, Via Sansone 1, 50019 Sesto Fiorentino (FI), Italy
[5] CNR – Institute for Photonics and Nanotechnologies, Via Trasea 7, 35131 Padua, Italy
[6] CISAS – Center of Studies and Activities for Space "Giuseppe Colombo", Via Venezia 15, 35131 Padua, Italy
[7] INAF – Capodimonte Astronomical Observatory, Salita Moiariello 16, 80131 Naples, Italy
[8] INAF – Istituto di Astrofisica Spaziale e Fisica Cosmica, Via Alfonso Corti 12, 20133 Milan, Italy
[9] INAF – Turin Astrophysical Observatory, Via Osservatorio 20, 10025 Pino Torinese (TO), Italy
[10] INAF – Catania Astrophysical Observatory, Via Santa Sofia 78, 95123 Catania, Italy
[11] Catholic University at NASA – GSFC, Maryland, USA
[12] INAF – Padua Astrophysical Observatory, Vicolo Osservatorio 5, 35122 Padua, Italy
[13] University of Urbino – Dipartimento di Scienze Pure e Applicate, Via Santa Chiara 27, I-61029 Urbino, Italy
[14] INFN – Istituto Nazionale di Fisica Nucleare, Section in Florence, Via G. Sansone 1, 50019 Sesto Fiorentino, Italy
[15] Astronomical Institute of the Czech Academy of Sciences, Fričova 28, 25165 Ondřejov, Czech Republic
[16] University of Wrocław, Center of Scientific Excellence – Solar and Stellar Activity, Kopernika 11, 51-622 Wrocław, Poland
[17] INAF – Trieste Astronomical Observatory, Via G.B. Tiepolo 11, 34143 Trieste, Italy
[18] Jet Propulsion Laboratory, California Institute of Technology, Pasadena, CA 91109, USA
[19] Politecnico di Torino, Corso Duca degli Abruzzi 24, 10129 Torino, Italy
[20] NASA Headquarters, Washington, DC 20546-0001, USA
[21] University of Padova – Physics and Astronomy Department "Galileo Galilei", Via F. Marzolo 8, 35131 Padua, Italy
[22] University of Padova – Department of Information Engineering, Via Gradenigo 6/B, 35131 Padova, Italy
[23] Italian Space Agency, Via del Politecnico, 00133 Rome, Italy